RESEARCH ARTICLE | JULY 23 2024

Does dispersed phase inertia affect the shape of sheared emulsion droplets?

Valentina Preziosi ; Anik Tarafder ; Giovanna Tomaiuolo ; Kausik Sarkar ; Stefano Guido

Physics of Fluids 36, 073115 (2024)
https://doi.org/10.1063/5.0219152

Physics of Fluids ARTICLE pubs.aip.org/aip/pof

Does dispersed phase inertia affect the shape of sheared emulsion droplets?

Cite as: Phys. Fluids **36**, 073115 (2024); doi: 10.1063/5.0219152
Submitted: 15 May 2024 · Accepted: 6 July 2024 ·
Published Online: 23 July 2024

Valentina Preziosi,[1,2] Anik Tarafder,[3] Giovanna Tomaiuolo,[1,2,a)] Kausik Sarkar,[3] and Stefano Guido[1,2]

AFFILIATIONS

[1]Dipartimento di Ingegneria Chimica, dei Materiali e della Produzione Industriale, Università di Napoli Federico II, 80125 Napoli, Italy
[2]CEINGE Biotecnologie avanzate Franco Salvatore, 80143 Napoli, Italy
[3]Department of Mechanical and Aerospace Engineering, The George Washington University, Washington, DC 20052, USA

[a)]Author to whom correspondence should be addressed: g.tomaiuolo@unina.it

ABSTRACT

Inertial effects on sheared emulsion droplets are a topic of scientific and industrial interest for several applications from processing to microfluidics. Most of the literature have addressed so far the role of inertia of the continuous phase, which is known to affect shear-induced droplet deformation and migration at values of the Reynolds number of the external fluid $\mathrm{Re_c} > 1$. However, less attention has been paid to the case of inertial effects inside the droplets, corresponding to values of the Reynolds number of the droplet fluid $\mathrm{Re_d} > 1$. Such a case is especially relevant when the viscosity ratio λ between the droplet and the external fluid is $\ll 1$, which is typical of water-in-oil emulsions where the low values of droplet viscosity can result in $\mathrm{Re_d} > 1$, while $\mathrm{Re_c} < 1$ due to the larger oil viscosity. Here, we focus on the effect of droplet inertia under shear flow at $\lambda \ll 1$ by high-speed video microscopy experiments in a microcapillary and by numerical simulations based on a front-tracking finite-difference method. The results unveil the droplet's three-dimensional shape under shear flow at low viscosity ratios and show that droplet inertia tends to increase droplet deformation and orientation along the flow direction and to form two vortices inside the droplets even at small Re_c. The latter findings are at variance with the case of external fluid inertia, where droplets become more aligned with the velocity gradient direction.

I. INTRODUCTION

Emulsions are ubiquitous in everyday life, from foodstuff to drugs and personal care products. In most applications, the properties of emulsions are highly dependent on the size distribution of the micrometer-scale droplets dispersed in the continuous phase. In turn, the size and shape of emulsion droplets are strongly affected by the flow conditions experienced during processing or usage. Hence, flow-induced deformation of droplets has been extensively studied in the literature, both theoretically and experimentally, with a special emphasis on model flow fields, such as simple shear, which can provide important insights into more complex flow conditions.[1,2] Most of the literature has been restricted to slow flows, where inertia can be neglected and droplet shape can be described in terms of two non-dimensional parameters: the capillary number Ca and the viscosity ratio λ. The former is the ratio between viscous stress acting to deform the droplet and interfacial stress tending to restore the spherical shape at rest, $Ca = (\dot{\gamma} R \mu_c)/\sigma$, where $\dot{\gamma}$ is the shear rate, R is the undeformed radius of the droplet, μ_c is the continuous phase viscosity, and σ is the interfacial tension. The viscosity ratio $\lambda = \mu_d/\mu_c$ (μ_d is the dispersed phase viscosity) is the other important parameter. Droplet shape is usually described in terms of two parameters: the deformation parameter, $D = (a - b)/(a + b)$, where a and b are the two droplet semiaxes in the shear plane, and the orientation angle θ, which is defined as the angle between the major axis a and the flow direction x. Analytical expressions for the deformation parameter and the orientation angle in the limit of small deformations were found by Taylor (to first order in Ca)[3] $D = Ca(19\lambda + 16)/(16\lambda + 16)$, and by Chaffey and Brenner (to second order in Ca)[4] $\theta = \pi/4 - Ca(19\lambda + 16)(2\lambda + 3)/(80\lambda + 80)$, respectively. Both expressions have been found to be in good agreement with experimental data up to moderate deformations, where the shape of a sheared droplet can be described as an ellipsoid under the slow flow (Stokes) approximation.[5]

In many industrial applications, however, such as in emulsion processing in stirred mixers, turbulent flow conditions are found, where inertia cannot be neglected, and the Reynolds number, expressing the ratio between inertial and viscous stresses, needs to be accounted for, in addition to Ca and λ, to describe droplet shape. The interaction of droplets with turbulent eddies is a complex problem in

fluid mechanics. As an example, the motion of a droplet in a potential vortex has been studied by numerical simulations based on a front-tracking finite difference method, and a rich and diverse dynamics has been found, including a resonance phenomenon when the natural frequency of the droplet matches the frequency of the forcing flow.[6,7] The deformation of sub-Kolmogorov-scale droplets has been investigated by direct numerical simulation of isotropic turbulence, showing the complex interplay between droplet shape and the local fluid velocity gradient tensor.[8,9] A similar approach has been used to investigate the effects of walls and of surfactants on droplet deformation in turbulent flows.[10,11] In addition, the effect of the Reynolds number on the deformation and breakup of a droplet has been studied by numerical simulations in special cases, such as a particulate shear flow[12] and an electric field.[13]

Although droplet shape in turbulent flows is a complex subject, some useful insight can still be obtained from simple shear flow as a representative of the flow field experienced by a droplet between two co-rotating eddies. Indeed, it has been shown[14] that the value of the Reynolds number of the continuous phase $Re_c = (\rho_c \dot{\gamma} R^2)/\mu_c$ (ρ_c is the density of the continuous phase) at the spatial scale of the droplet size (1–100 μm) is in the range between 0.01 and 100 under typical well-developed turbulent conditions in a stirred water-based liquid–liquid system. Hence, while interacting with turbulent eddies in such conditions, the droplet experiences low to moderate values of the Reynolds number, which has been the focus of most studies concerning droplet shape in simple shear flow including the effect of inertia.[15] One of the main results from the literature is that inertia acts to rotate the drop toward the velocity gradient direction.[16,17] It has been suggested that the rotation is due to the formation of vortical swirls at the two ends of the droplet,[18] whose large velocities are associated with negative pressures according to Bernoulli's equation, thus tilting the droplet with a suction mechanism analogous to the aerodynamic lift. In this way, the droplet is subjected to a larger shear deformation in the flow direction pulling the ends away from each other and tends to break up at lower critical capillary numbers with increasing Re_c.

The topic of droplet breakup under shear with continuous phase inertia has also received considerable attention. It was shown that in the presence of inertia, droplet breakup occurs at values of λ beyond the threshold of about 3.7, which is found under a Stokes flow condition.[19] Other inertia-induced phenomena in a shear flow concern the distribution of drop fragments resulting from breakup,[20] effects of geometrical confinement,[21,22] the change in the sign of the first and second normal stress difference of a dilute emulsion,[23] and reversed streamlines and streamlines spiraling around the vorticity axis.[17] From the experimental side, droplet breakup in turbulent flow has been the subject of several studies based on high-speed flow visualization.[24–29] The role of surfactants on droplet breakup in a turbulent flow has been also investigated by experiments.[30]

Most of the above-mentioned studies have focused on viscosity ratios around 1 or larger. The range of λ between 0.1 and 2 at $Re_c = 10$ has been explored numerically in Ref. 31 by a diffuse interface free energy lattice Boltzmann method, and it was found that the droplets are less elongated and more oriented toward the vertical axis at increasing λ. From the experimental side, works on the deformation of single droplets in simple shear flow at non-negligible values of Re_c are essentially lacking in the literature, the few available studies being addressed to statistical quantities of emulsions, such as the distribution of droplet size in emulsification devices at λ around 1 or higher.[32]

However, if one considers water in oil emulsions, they are often characterized by values of $\lambda \ll 1$, a case which has been neglected in the literature. It can be noticed that, even for low inertia in the continuous phase, i.e., for $Re_c < 1$, due to the low viscosity ratio, the droplet-based Reynolds number $Re_d = (\rho_d \dot{\gamma} R^2)/\mu_d = \mathrm{Re}_c/\lambda > 1$. For example, for $\lambda = 0.01$ and $Re_c = 0.1$, $Re_d = 10$, and the question arises about the effects of droplet inertia on deformation. Our work is addressed at the latter question both by high-speed video microscopy experiments in a microcapillary and by numerical simulations based on a front-tracking finite-difference method. We focus on dilute water-in-oil emulsions at $\lambda = 0.01$, where droplet interactions can be neglected, and the flow behavior of an isolated droplet is representative of the emulsion as a whole. The results are expressed in terms of the three axes and the orientation angle of the droplet, as well as the deformation parameter as a function of the capillary number. Furthermore, numerical simulations are exploited to extend the range of parameter values and to obtain additional quantities, such as the surface rotation and the internal circulation of the droplet, which are not easily accessible by experimental techniques.

II. MATERIALS AND METHODS

A. Experimental

Two emulsions have been investigated, with the same viscosity ratio but exhibiting different viscosities of the two phases, as specified in Table I. One has been obtained by mixing bi-distilled water (dispersed phase) with soybean oil ($\mu_c = 0.06$ Pas and $\rho_c = 0.917$ g/cm^3). The equilibrium value of the interfacial tension, measured using the pendant drop technique, is 29 mN/m.[33] The viscosity ratio $\lambda = \mu_d/\mu_c$, where μ_d is the dispersed phase viscosity, is 0.017, and the aqueous dispersed phase volume fraction is kept around 5% to reduce droplet–droplet interactions and coalescence.[34,35] The other emulsion with the same viscosity ratio is obtained by using polydimethylsiloxane (PDMS purchased from Carl Roth, $\mu_d = 0.097$ Pa s, and $\rho_d = 0.975$ g/ml) dispersed in polybutene (PIB, Indopol H-50 purchased from Ineos Oligomers $\mu_c = 8.3$ Pa s, $\rho_c = 0.895$ g/cm^3), with an interfacial tension of 2.8 mN/m.

A microfluidic approach allowed us to obtain the three-dimensional shape of single droplets in a dilute emulsion under shear flow. As shown in Fig. 1(a), a water-in-oil emulsion is fed by a syringe pump (Harvard 11 Plus) to a circular cross section silica capillary (with inner diameter of 320 μm, Polymicro Technologies, Phoenix, AZ, USA) placed on the motorized x–y stage (Ludl, Hawthorne, NY, USA) of an inverted microscope (Axiovert 100-Zeiss). More details on the apparatus can be found elsewhere.[36] Individual droplets close to the capillary wall are observed by a high-speed camera (Phantom 4.3) able to acquire up to a thousand frames per seconds and a high magnification objective (Zeiss Plan-Neofluar, 40x/1.3 oil). Images of the

TABLE I. Properties of the systems investigated.

System	Phase	μ (Pa s)	ρ (g/ml)	σ (mN/m)
Water in soybean oil	Dispersed	0.001	1	29
	Continuous	0.06	0.917	
PDMS in PIB	Dispersed	0.097	0.975	2.8
	Continuous	8.3	0.895	

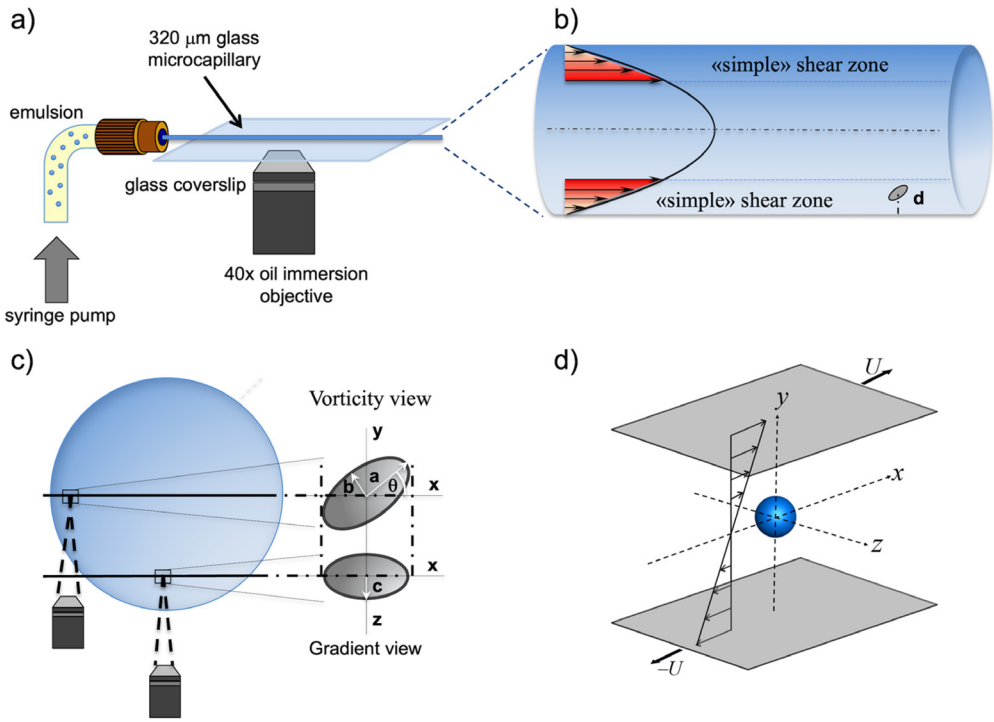

FIG. 1. (a) Schematic of the microfluidic experimental setup. (b) Sketch of the velocity profile with the quasi-simple shear zone near the walls. (c) Droplet shapes in the *x*–*y* (vorticity) and *x*–*z* (velocity gradient) planes are obtained by focusing the microscope at the midplane and close to the wall of the capillary cross section, respectively; a, b and c are the semi-axes, θ is the orientation angle, and d is the distance between droplet center and wall. (d) Schematic of the computational setup.

droplets flowing inside the microcapillary have been acquired at a rate (from 10 to 3000 fps) depending on the imposed flow. They were analyzed by image analysis techniques by using a commercial software package (Image Pro-Plus). With this setup, shear rates high enough to induce significant droplet deformations can be reached, while avoiding buoyancy effects (the ratio between gravitational and shear forces $\frac{\Delta\rho g R}{\mu_c \dot{\gamma}} \ll 1$). The flow of the continuous phase can still be taken as laminar since $Re_c \ll 1$ (e.g., for $\dot{\gamma} = 12\,700\ \mathrm{s}^{-1}$, which is the highest value in the experiments, and $R = 10\ \mu$m, $Re_c = 0.02$, while $Re_d = 1.3$).

Concerning the image processing, droplet selection was carried out due to the presence of (undesired) droplets either out of focus or out of the simple shear zone. The analysis of the selected droplets in the field of view was then performed in a semi-automated way (i.e., by choosing a gray level threshold to capture the droplet's contour). In particular, the following geometrical parameters were measured: droplet axis (*a*, *b*, *c*), distance *d* between the droplet center of mass and the capillary wall and the droplet velocity, *v*. The latter were used to calculate the local shear rate as $\dot{\gamma} = v/d$. About 100 droplets were analyzed at each flow rate.

As shown by Li and Pozrikidis,[37] the flow of a droplet in a tube can be approximated to simple shear if droplet radius *R* is sufficiently small compared to the tube radius r (i.e., R/r < 0.1) and the distance of the droplet from the wall is ∼5*R* to avoid confinement effects[33] [see Fig. 1(b)]. In this work, we exploit this microfluidics setup to image the flowing droplets both in the shear plane [*x*–*y* in Fig. 1(c)] and along the vorticity gradient [*x*–*z* in Fig. 1(c)] by changing the microscope focus and the observation window [Fig. 1(c)]. Two independent, perpendicular views are acquired and, by matching the corresponding droplet contours, its three-dimensional shape was obtained. Droplet contours in the two planes are matched (and thus identified as if corresponding to the same droplet) when the projection of the *a*-axis is equal to the long axis in the *x*–*z* plane. All the measurements of droplet shape have been done by using a commercial image analysis software (Image Pro Plus, Media Cybernetics).

From the experimental point of view, the investigation of the effects of droplet inertia in water in oil emulsions is beset by several difficulties, such as small size of droplets (usually in the 1–10 μm range), buoyancy due to the density difference, which leads to phase separation, and high values of shear rate needed to deform a droplet from the spherical equilibrium shape due to the low viscosities of water and oil. The lower μ_c is, the higher is $\dot{\gamma}$ required to have a significant value of *Ca* and thus of droplet deformation. For example, to reach *Ca*∼0.1 with typical values of $R = 10\ \mu$m, $\mu_c = 50$ mPa s, $\sigma = 10$ mN/m, $\dot{\gamma}$ should be of the order of $10^3\ \mathrm{s}^{-1}$, which is difficult to achieve at the single droplet level with conventional laboratory instrumentation.

B. Numerical simulation

The system is governed by incompressible momentum conservation equations in the entire domain Ω,

$$\frac{\partial(\rho\mathbf{u})}{\partial t} + \nabla\cdot(\rho\mathbf{u}\mathbf{u}) = \nabla\cdot\boldsymbol{\tau} - \int_{\partial\mathbf{B}} d\mathbf{x}_\mathbf{B}\kappa\mathbf{n}\Gamma\delta(\mathbf{x}-\mathbf{x}_\mathbf{B}), \quad (1)$$

$$\nabla\cdot\mathbf{u} = 0. \quad (2)$$

The total stress $\boldsymbol{\tau}$ is written as $\boldsymbol{\tau} = -p\mathbf{I} + \mu\mathbf{D}$, where p is the pressure, $\mathbf{I}$ is the identity tensor, μ is the drop-fluid system viscosity, and $\mathbf{D} = (\nabla\mathbf{u}) + (\nabla\mathbf{u})^T$ is twice the deformation rate tensor. μ takes the value of μ_d in the drop phase and that of μ_c in the continuous phase. The last term of Eq. (1) describes interfacial tension at the drop surface $\mathbf{x_B}$, Γ is the interfacial tension (constant), $\partial\mathbf{B}$ represents the surface of the drop, κ is the local curvature, $\mathbf{n}$ is the outward normal, and $\delta(\mathbf{x} - \mathbf{x}_B)$ is the three-dimensional Dirac delta function. The presence of the surface tension introduces a jump in normal stress across the interface represented by the delta function. A smooth representation of the delta function is used for the numerical front-tracking implementation. The drop surface was discretized with triangular elements resulting in a Lagrangian front grid separate from the three-dimensional Eulerian volume grid. The front-tracking method was originally developed by Tryggvason and coworkers[38] using a single fluid formulation for the multiphase flow in the entire domain, with parameters such as viscosity and density changing sharply but smoothly over a few grid spacings across the interface between fluids. The material properties are represented as

$$\begin{aligned} \rho(\mathbf{x}) &= \rho_c + (\rho_d - \rho_c)J(\mathbf{x}), \\ \mu(\mathbf{x}) &= \mu_c + (\mu_d - \mu_c)J(\mathbf{x}), \end{aligned} \tag{3}$$

where

$$J(\mathbf{x}) = \begin{cases} 1, & \mathbf{x} \in \Omega_d, \\ 0, & \mathbf{x} \in \Omega_c. \end{cases} \tag{4}$$

The numerical method uses a smooth representation of the indicator function $J(\mathbf{x})$. The velocity on the drop surface is related to the surrounding fluid as

$$\mathbf{u}(\mathbf{x_B}) = \int_\Omega \delta(\mathbf{x} - \mathbf{x_B})\mathbf{u}(\mathbf{x})d\mathbf{x} \tag{5}$$

with a corresponding smooth representation of the delta function. Once the velocities on the drop elements are identified, the points in the drop surface are advected as

$$\frac{d\mathbf{x_B}}{dt} = \mathbf{u}(\mathbf{x}). \tag{6}$$

A smooth representation of the δ–function was achieved by using the Peskin interpolation.[39] Essentially, the fluid properties vary sharply but continuously over $4\Delta x$ Eulerian grid points as

$$\delta(\mathbf{x} - \mathbf{x_B}) = \delta^1(x - x_B)\delta^1(y - y_B)\delta^1(z - z_B), \tag{7}$$

where

$$\delta^1(x - x_B) = \frac{1}{4\Delta x}\left(1 + \cos\frac{\pi}{2\Delta x}(x - x_B)\right), \qquad |x - x_B| \le 2\Delta x. \tag{8}$$

The momentum equation is solved on a staggered grid with an operator splitting projection finite difference method.[40] A semi-implicit alternating direction implicit (ADI) scheme was adopted to alleviate restrictions on time-stepping ($\Delta t < \rho(\Delta x)^2/6\mu$). The time step nondimensionalized by the inverse shear rate for our simulations is 10^{-4}. A multi-grid solver was used to solve the pressure Poisson equation. The code has been validated extensively with benchmark problems and numerous single and multi-drop simulations.[6,40–42] The details can be found in our previous articles.[43,44] For the completeness of this manuscript, in Sec. II B 1, we provide a grid convergence, domain adequacy, and dispersed phase Reynolds number study of the code.

To numerically solve the problem, initially, a drop of radius R is placed in the center of the computational domain of size $L_x = 10R$, $L_y = 10R$, and $L_z = 5R$ [Fig. 1(d)], which has been found to be sufficient to neglect any wall effect (see Sec. II B 1). The computational domain was discretized with $128 \times 128 \times 64$ uniform cartesian grid points in the x, y, and z directions, respectively (grid independence study in Sec. II B 1). The top and the bottom walls in the y-direction moved with equal and opposite velocity U to create a uniform shear rate of strength $\dot{\gamma} = 2U/L_y$. Periodic boundary conditions were applied in the x (flow) and z (vorticity) directions. A fully developed shear flow was assumed at $t = 0$. Flow parameters are nondimensionalized, with the drop radius R as the length scale and inverse shear rate as the timescale. The Reynolds number, $Re_c = \rho_c\dot{\gamma}R^2/\mu_c$, capillary number, $Ca = \dot{\gamma}R\mu_c/\sigma$, viscosity ratio $\lambda = \mu_d/\mu_c$, and $Re_d = Re_c/\lambda$ are the main non-dimensional numbers governing the problem. To be consistent with the experiment, the velocity U of the top wall and bottom wall is varied to attain various strengths of shear rates leading to various Ca and Re_d. For other sets of simulation, Re_d has been kept constant, and the interfacial tension has been varied to achieve different Ca to compare with the former one. The density ratios between the dispersed and continuous phases for both the water in soybean oil and PDMS in the PIB system are ~1.09. Thus, the density ratio for the numerical simulations is kept at 1 for all the cases. The viscosity ratio has been kept at 0.01 to achieve higher inertia inside the drop. From the numerical side, the simulation of an extremely low viscosity ratio is also hindered by several challenges. Because of the explicit time stepping used in the code here, instead of Stokes flow, we keep Re_c at a low but finite value of 0.01 and decrease the viscosity ratio to achieve a higher Reynolds number inside the drop. The code is an MPI-based fully parallelized solver, and it is run on the George Washington University's HPC cluster PEGASUS. In the following, we plot the drop shapes using the front geometry. We compute the major (a/R) and the minor (b/R) axes of the drop by determining its maximum and the minimum dimensions, which in the present case of plane shear are in the x–y plane. The c/R is distance from the drop center of the point with the maximum z-dimension. The period of rotation for a point at the drop surface is computed by noting how long it takes for a vertex on the drop surface complete one rotation.

1. Grid, domain independence, and dispersed phase Reynolds number

The code has been extensively validated against experimental and numerical results in the literature involving single and multiple drops in shear. For instance, in Ref. 23 (Fig. 3 there), we successfully compared the lengths of the three axes of the deformed drop in shear with experimental observations of Refs. 45 and 46; in Ref. 17 (Fig. 2 there), we compared detailed geometry of the inertia induced streamlines between our simulation and computations of Refs. 47 and 48; and in Ref. 49 (Fig. 4 there), we compared our simulation of drop trajectories in a shear-induced pair-interaction with experimental observation of Ref. 50. Here, for the sake of completeness, we offer a brief study of the grid and domain dependence and show that $Re_c = 0.01$ is an adequate proxy for smaller Re_cs obtained in the experiments here. In Fig. 2(a),

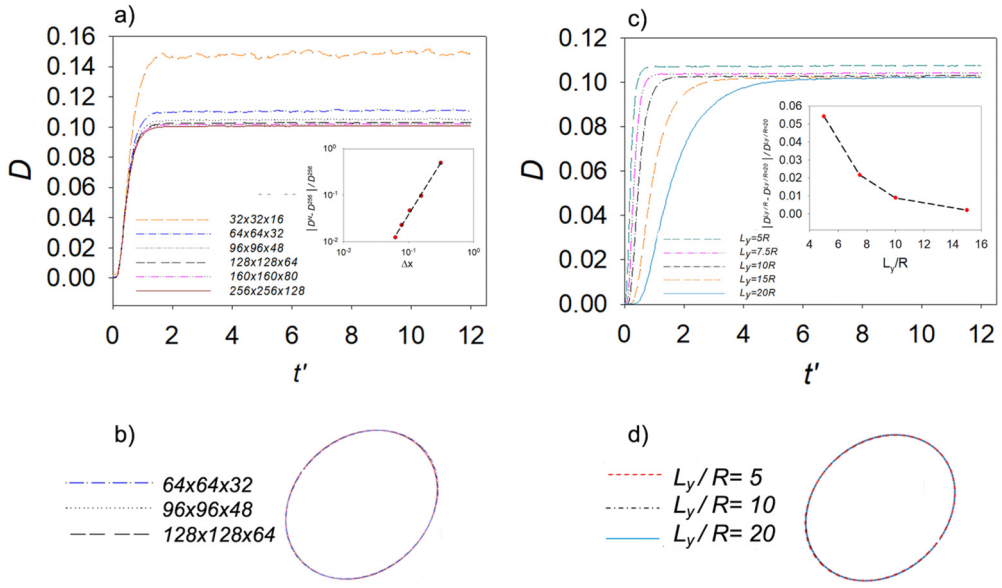

FIG. 2. (a) Droplet deformation for six different grid resolutions at Ca = 0.1, $\lambda = 0.01$, and $Re_d = 10$. The inset shows relative error plotted against grid sizes and (b) corresponding droplet shapes for three grid resolutions. (c) Droplet deformation for five different domain sizes in the velocity gradient directions. The inset shows relative error plotted against domain sizes and (d) corresponding droplet shapes. Flow parameters are the same as (a).

we plot droplet deformation for six different grid resolutions in a computational domain of size $L_x = 10R$, $L_y = 10R$, and $L_z = 5R$. The capillary number is $Ca = 0.1$, viscosity ratio $\lambda = 0.01$, and $Re_d = 10$ for all the cases. For all the grid resolutions, the droplet deforms to an ellipsoidal shape and eventually attains a steady deformation. The droplet deformation decreases with the increase in grid refinement, and the successive difference between corresponding droplet deformation reduces. In the inset of Fig. 2(a), we plot the relative error of the steady state droplet deformation against grid size, showing a rate of convergence close to second order (~ 1.7). The droplet shape [Fig. 2(b)] also does not show a significant difference with grid refinement. An increase in the grid resolution from $128 \times 128 \times 64$ to $256 \times 256 \times 64$ changes the drop deformation by less than 3%. Thus, we choose $128 \times 128 \times 64$ for all our numerical simulations in Sec. III. In Fig. 2(c), we plot the droplet deformation for five different domain sizes (L_y/R) to ensure no effects from the walls in the velocity gradient direction. Domain sizes of $5R$ and $7.5R$ have a strong effect on the steady state drop deformation; however, the effect starts to become negligible with further increase. The increase in the domain size from $10R$ to $20R$ changes the drop deformation by less than 1% [Fig. 2(c) inset]. Corresponding drop shapes also show insignificant differences [Fig. 2(d)]. We choose $L_y = 10R$ for all simulations.

In Fig. 3(a), we plot the magnitude of the shear rate $\sqrt{\mathbf{D} : \mathbf{D}/2}$ to show a typical flow field from the simulation. Here, $\mathbf{D}$ is twice the deformation rate tensor as described in Sec. II B. Locally, the shear rate is higher along the extensional and compression regions, where the maximum value is observed along the extensional region. A lower magnitude of shear rate is observed on the top, bottom, front, and back of the droplet surface. Far from the droplet, the magnitude is equal to the applied nondimensional shear rate ($\sim$1). In the numerical simulations, because of the explicit time stepping, the lowest Re_c is restricted to 0.01 although experiments were performed for values, as low as 10^{-6}, effectively a Stokes flow. In Fig. 3(b), we plot the steady state drop deformation against continuous phase Reynolds number Re_c. The steady state droplet deformation and droplet shapes [Fig. 3(c)] do not change significantly for the Reynolds numbers ranging from 0.01 to 0.1, indicating that $Re_c = 0.01$ is a sufficient proxy for lower Re_c.

III. RESULTS

Representative images of droplet shape along the vorticity and the velocity gradient axes are shown in Fig. 4, both from experiments (left) and simulations (right).

The images in Fig. 4 (left panel) (a)–(c) refer to water droplets in soybean oil at increasing values of Ca and Re_d obtained by increasing the flow rate and thus the wall shear rate, which takes values of several thousands of reciprocal seconds. Under such conditions, Re_d is close to 1, and the droplet appears quite deformed and oriented already at $Ca = 0.06$. The view along the velocity gradient [Fig. 4 left panel: (a′)–(c′)] shows large droplet deformation as well. The images in Fig. 4 (left panel) (d)–(f) refer to PDMS droplets in PIB at the same value of the viscosity ratio but at negligible Re_d. In these conditions, droplets are less deformed at similar values of Ca with respect to water droplets in soybean oil, as can also be seen in the view along the velocity gradient [Fig. 4 left panel (d′)–(f′)]. Similar qualitative results are found by numerical simulations, which are shown in Fig. 4 (right panel).

A quantitative analysis of droplet shape is shown in Fig. 5, where the three semi-axes, normalized with respect to the droplet radius, are plotted as functions of Ca for the two emulsions, both from the experiments and the numerical simulations.

In the plot, star full symbols correspond to the PDMS in the PIB system, which exhibits negligible values of Re_d. The data of a/R (green stars), b/R (red stars), and c/R (blue stars) are well represented by the

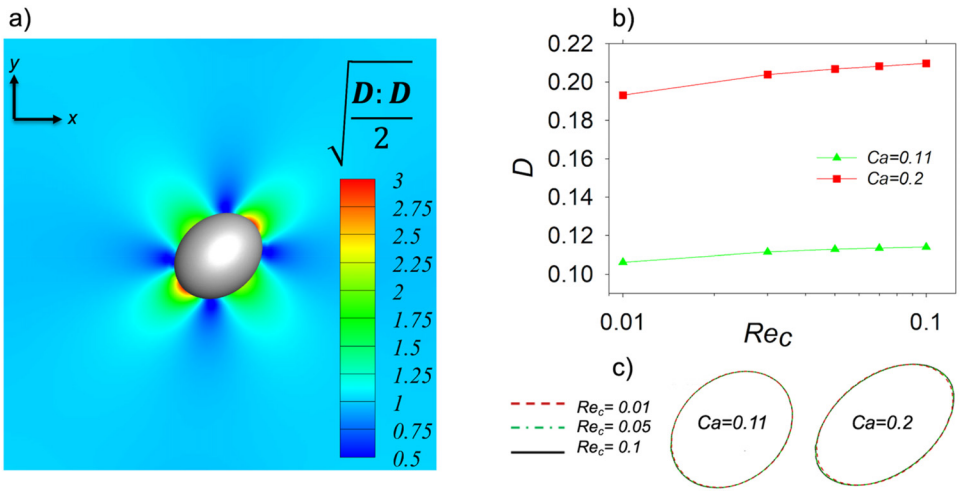

FIG. 3. (a) Contour of the shear rate magnitude for Ca = 0.1 and $Re_d = 10$. (b) Steady state droplet deformation vs continuous phase Reynolds number ($Re_c = \lambda Re_d$) for Ca = 0.2 and Ca = 0.11. (c) Droplet shapes at Ca = 0.2 and Ca = 0.11.

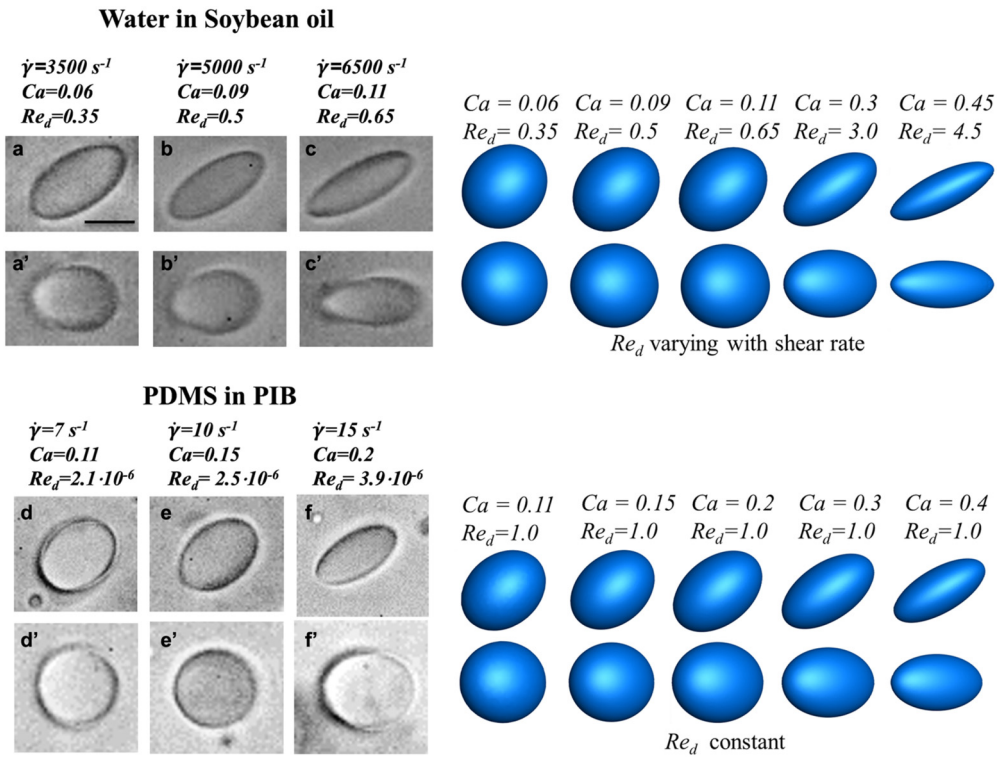

FIG. 4. Representative images of sheared droplets along the *x*–*y* (vorticity) and *x*–*z* (velocity gradient) planes from experiments (left) and numerical simulations (right). (Left panel) Droplet images for the water in soybean oil system along the *x*–*y* plane (a)–(c) and *x*–*z* (a′)–(c′) plane at increasing shear rate. Droplet images for PDMS in PIB along the *x*–*y* plane (d)–(f) and *x*–*z* (d′)–(f′) plane at increasing shear rate. Scale bar is equal to 10 μm. (Right panel) Droplet images (top from *x*–*y* plane and bottom *x*–*z* plane) from numerical simulations at various Ca and Re_d conditions. For the numerical results, $\lambda = 0.01$ and $Re_c = \lambda\, Re_d$.

predictions of the second-order small deformation theory (dashed, dot-dashed, and continuous lines, respectively). A quite different behavior is exhibited by the water in soybean oil system (upper full triangles in Fig. 5). Here, a remarkable deviation from the theory predictions is shown by the data of *a/R*, which are above the dashed line, especially at *Ca* between 0.1 and 0.2. This finding is in line with the elongated shapes of Fig. 4 left panel (a)–(c). The data of the third axis *c/R*, too, do not follow the theory predictions and essentially

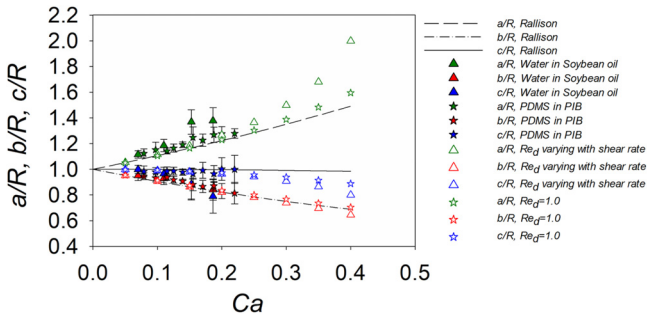

FIG. 5. The three normalized droplet semi-axes vs Ca from experiments full points and numerical simulations (empty points). The experimental data refer to water in soybean oil (upper triangles), with Re_d up to 1.3, and PDMS in PIB (stars), with Re_d around 2×10^{-6}. The numerical results are represented by empty stars ($Re_d = 1$) and empty triangles (Re_d varying with shear rate from 5 to 40) symbols. The lines correspond to the predictions of the second-order small deformation theory. For the numerical results, $\lambda = 0.01$ and $Re_c = \lambda\, Re_d$.

overlap with the data of b/R, thus showing a flattening of the droplet shape, which can be seen in the images of Fig. 4 left panel: (d′)–(f′). Such flattening is similar to previous data from the literature for $\lambda < 1$ and high Ca, where inertia was negligible and flattening was due to the dominant effect of viscosity over interfacial tension.[51]

The results of the numerical simulations are in qualitative agreement with the experiments, as shown by the plot of Fig. 5. The calculated values of the semi-axis a/R at varying Re_d tend to become larger than the ones at small Re_d (dashed line), with a stronger deviation at $Ca > 0.2$. The quantitative difference between experimental and numerical results can be attributed to the difficulties associated with a value of $\lambda \ll 1$. The numerical simulations allow to extend the range of values of Ca experimentally accessible, which is limited to about 0.25 in our setup. In fact, the velocity of the droplets at larger values of Ca makes imaging more challenging due to motion-induced blurring.

The semi-axis data of Fig. 5 have been used to calculate the deformation parameter D, which is shown in Fig. 6(a), together with the orientation angle θ(b), as functions of the capillary number.

The experimental data of the deformation parameter in Fig. 6(a) confirm the findings already discussed. While the PDMS in the PIB system follows the classical linear prediction of Taylor theory, larger values of D are found for water in soybean oil at values of Ca between 0.1 and 0.2. A similar trend is also found in the numerical simulations of Fig. 6(a), with a slight deviation in D from the linear theory at larger values of Ca. For the PDMS in the PIB system, the orientation angle in Fig. 6(b) is well described by the predictions of the second-order Chaffey–Brenner theory (equation reported in the Introduction). Although the measurement of the orientation angle is affected by a larger experimental error for the water in soybean oil system due to image blurring at high droplet velocity, the data show a clear downward deviation from the second-order predictions, in qualitative agreement with the numerical simulations. Thus, at values of Re_d around 1 ($Ca \sim 0.2$) and above, droplets are more oriented along the flow direction with respect to the case of negligible inertia.

Further insight on the results found so far can be obtained by looking at the rotation of the interface in the equatorial plane and at flow inside the droplet. The circulation number $m = T\dot{\gamma}/(4\pi)$, where T is the period of rotation of a tracer on the droplet interface in the equatorial plane, is plotted in Fig. 7(a) as a function of Ca for $\lambda = 1$. In Fig. 7(a), the symbols represent numerical simulations, and the dashed line is the prediction of the small deformation theory.

The latter has been calculated from the following equation:[52]

$$m = \frac{\lambda+1}{\sqrt{\lambda(\lambda+2)}} + \frac{95\lambda(19\lambda+16)}{4\left[(19\lambda)^2 + (20/Ca)^2\right]}\left[5 - \frac{(\lambda+1)(25\lambda^2+50\lambda-31)}{5\sqrt{\lambda^3(\lambda+2)^3}}\right]. \quad (9)$$

The good agreement between theory and numerical simulations provides a further validation of the latter. No comparison with experimental data could be made since it was not possible to measure the period of rotation in our experimental conditions. The increase in m with Ca, i.e., a slowing down of interface rotation at $\lambda = 1$, is associated with an increased droplet deformation and orientation along the flow

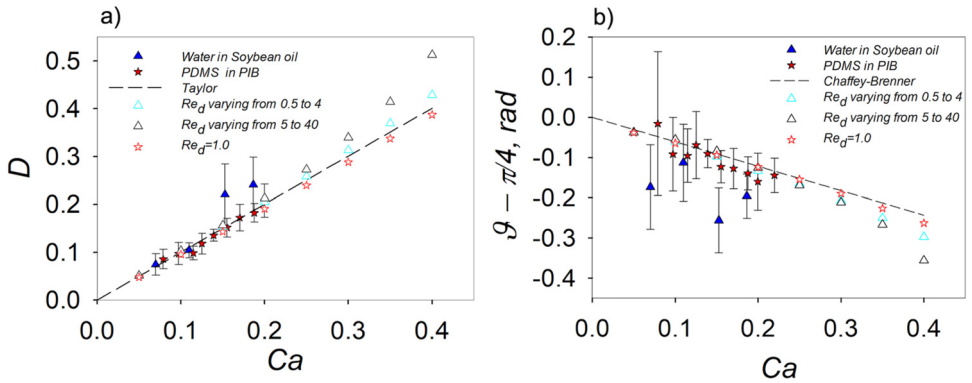

FIG. 6. (a) The deformation parameter D vs Ca from experiments and numerical simulations, respectively. (b) The orientation angle θ as a function of Ca from experiments and numerical simulations, respectively. The continuous and dashed lines are predictions of Eqs. (1) and (2) from the second-order small deformation theory. Re_d varies from 2×10^{-6} to 1.3 in the experiments and from 0.5 to 40 in the numerical simulations. For the numerical results, $\lambda = 0.01$ and $Re_c = \lambda Re_d$.

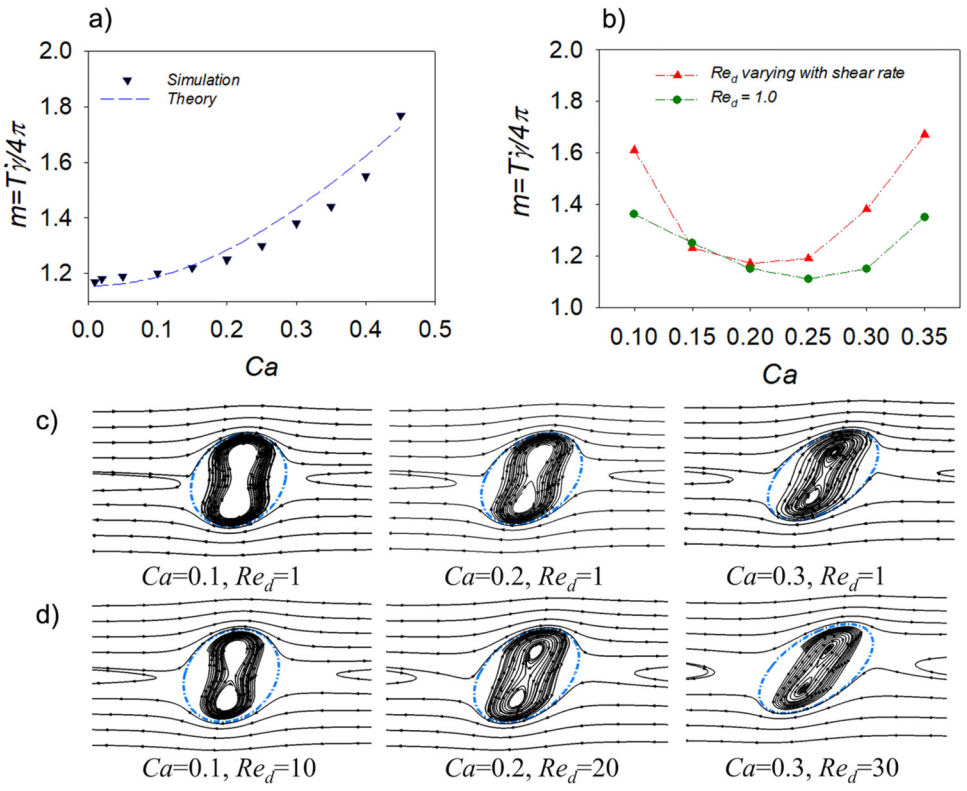

FIG. 7. (a) The circulation number m as a function of Ca at $\lambda = 1$ from numerical simulations in the Stokes limit; the dashed line is the prediction of the small deformation theory [Eq. (3)]. (b) The circulation number m as a function of Ca; the dashed line is a guide to the eye at $\lambda = 0.01$. (c) Streamlines from numerical simulations for different values of Ca and $Re_d = 1.0$. (d) Streamlines from numerical simulations for different values of Ca and Re_d. $\lambda = 0.01$ for (b)–(d) and $Re_c = \lambda\, Re_d$.

direction. The dependence of the circulation number on *Ca* changes at a viscosity ratio of 0.01, as shown in Fig. 7(b) for Re_d varying from 1 to 3.5 (here the line is just a guide to the eye and the predictions of the small deformation theory are not included in the plot since low values of λ are outside the range of validity of the theory). At such low values of λ, the circulation number m first decreases and then increases with the capillary number, reaching a minimum around $Ca = 0.2$. This behavior can be explained by the droplet internal circulation at $\lambda = 0.01$, which is shown in Fig. 7(c) for $Re_d = 1.0$ and in Fig. 7(d) for Re_d varying from 10 to 30. The images of the internal streamlines in the former case show the emergence of two vortices inside the droplet, which occurs around $Ca = 0.25$. For non-negligible droplet inertia, as shown in Fig. 7(d), the two vortices develop earlier, at $Ca = 0.2$, and persist at larger values of *Ca*. Indeed, the onset of the two vortices inside the droplets takes place at the same values of *Ca* as the ones corresponding to the minima in Fig. 7(b). Since at larger values of *Ca*, the circulation number m increases, droplet rotation slows down correspondingly, leading to an increased droplet deformation and orientation along the flow direction. This behavior is at variance with the case of inertial flow in the continuous phase, where the droplet is more oriented along the velocity gradient direction due to the formation of vortical swirls at the two ends of the droplet. Our results show that inertial effects inside the droplet, which are associated with the formation of two inner vortices, should be taken into account for shear flow at low viscosity ratios, even if the values of Re_c are rather small (i.e., for negligible inertia of the continuous phase).

IV. CONCLUSIONS

The focus of this work is the study of inertial effects inside a droplet under shear flow at a low viscosity ratio, a problem which has been overlooked in the literature in spite of its potential applications. The condition of non-negligible Re_d and $\lambda \ll 1$ is quite challenging to investigate both from the experimental and the numerical side. Hence, our approach is based on combining two advanced techniques, one experimental (high-speed flow visualization) and the other numerical (front-tracking finite-difference simulations), which complement and corroborate each other. In this way, we show that droplet deformation and orientation are larger as compared to the case of Stokes flow. This result can be interpreted in terms of the emergence of two vortices inside the sheared droplet, which start developing at lower values of *Ca* for larger values of Re_d (Fig. 7) and slow down the internal fluid circulation.

These findings provide some insight into the effects of shear flow on the 3D shape of droplets of dilute water-in-oil emulsions, which are associated with low viscosity ratios and are found in a number of applications, from industrial processing to microfluidics. In such emulsions, Re_c can exhibit low values even at high velocities due to the large viscosity of the oil, whereas Re_d can take values greater than 1 due to the

low viscosity of the water droplets. As a consequence, inertial effects inside the droplet become significant and can have important implications on the flow behavior of emulsions. As an example, the increased deformation experienced by the droplets at larger Re_d can promote their breakage in emulsification processes. Potential applications of our results can be found in the field of microfluidics, where the near-wall velocity field can be approximated by simple shear flow between parallel plates. Moreover, the large shear rate at the wall can lead to non-negligible inertial effects inside the droplets. Future work can be addressed to overcome the limits of our experimental setup and explore larger values of *Ca*, where droplet breakup is expected to take place. The effect of surfactants on droplet deformation and breakup in mixing devices, where inertial effects can be quite remarkable, can be investigated as well. Indeed, the fluid circulation inside the droplet can affect the distribution of surfactants on the droplet interface, an interesting topic for industrial applications.

AUTHOR DECLARATIONS

Conflict of Interest

The authors have no conflicts to disclose.

Author Contributions

Valentina Preziosi and Anik Tarafder contributed equally to this work.

Valentina Preziosi: Conceptualization (equal); Data curation (equal); Formal analysis (equal); Investigation (equal); Methodology (equal); Writing – original draft (equal); Writing – review & editing (equal). **Anik Tarafder:** Data curation (equal); Formal analysis (lead); Software (lead); Writing – original draft (equal); Writing – review & editing (equal). **Giovanna Tomaiuolo:** Conceptualization (equal); Data curation (equal); Formal analysis (equal); Investigation (equal); Methodology (equal); Writing – original draft (equal); Writing – review & editing (equal). **Kausik Sarkar:** Formal analysis (lead); Supervision (lead); Writing – original draft (equal); Writing – review & editing (lead). **Stefano Guido:** Conceptualization (equal); Supervision (lead); Writing – original draft (lead); Writing – review & editing (lead).

DATA AVAILABILITY

The data that support the findings of this study are available within the article.

REFERENCES

[1]H. A. Stone, "Dynamics of drop deformation and breakup in viscous fluids," Annu. Rev. Fluid Mech. **26**, 65 (1994).
[2]A. J. Wagner and J. Yeomans, "Effect of shear on droplets in a binary mixture," Int. J. Mod. Phys. C **8**, 773 (1997).
[3]G. I. Taylor, "The formation of emulsions in definable fields of flow," Proc. R. Soc. London Ser. A **146**, 501 (1934).
[4]C. E. Chaffey and H. Brenner, "A second-order theory for shear deformation of drops," J. Colloid Interface Sci. **24**, 258 (1967).
[5]S. Guido and M. Villone, "Measurement of interfacial tension by drop retraction analysis," J. Colloid Interface Sci. **209**, 247 (1999).
[6]K. Sarkar and W. R. Schowalter, "Deformation of a two-dimensional drop at non-zero Reynolds number in time-periodic extensional flows: Numerical simulation," J. Fluid Mech. **436**, 177 (2001).
[7]X. Li and K. Sarkar, "Drop deformation and breakup in a vortex at finite inertia," J. Fluid Mech. **564**, 1–23 (2006).
[8]P. Perlekar, L. Biferale, M. Sbragaglia, S. Srivastava, and F. Toschi, "Droplet size distribution in homogeneous isotropic turbulence," Phys. Fluids **24**, 065101 (2012).
[9]L. Biferale, C. Meneveau, and R. Verzicco, "Deformation statistics of sub-Kolmogorov-scale ellipsoidal neutrally buoyant drops in isotropic turbulence," J. Fluid Mech. **754**, 184 (2014).
[10]A. Roccon, M. De Paoli, F. Zonta, and A. Soldati, "Viscosity-modulated breakup and coalescence of large drops in bounded turbulence," Phys. Rev. Fluids **2**, 083603 (2017).
[11]G. Soligo, A. Roccon, and A. Soldati, "Breakage, coalescence and size distribution of surfactant-laden droplets in turbulent flow," J. Fluid Mech. **881**, 244 (2019).
[12]A. Ardekani, S. Dabiri, and R. Rangel, "Deformation of a droplet in a particulate shear flow," Phys. Fluids **21**, 093302 (2009).
[13]B. Nath, G. Biswas, and A. Dalal, "Influence of electric field on deformation of a drop in shear flow," Phys. Fluids **31**, 042102 (2019).
[14]A. Komrakova, O. Shardt, D. Eskin, and J. Derksen, "Lattice Boltzmann simulations of drop deformation and breakup in shear flow," Int. J. Multiphase Flow **59**, 24 (2014).
[15]P. Olad, F. Innings, M. Crialesi-Esposito, L. Brandt, and A. Håkansson, "Comparison of turbulent drop breakup in an emulsification device and homogeneous isotropic turbulence: Insights from numerical experiments," Colloids Surf. A **657**, 130569 (2023).
[16]Y. Y. Renardy and V. Cristini, "Effect of inertia on drop breakup under shear," Phys. Fluids **13**, 7–13 (2001).
[17]R. K. Singh and K. Sarkar, "Inertial effects on the dynamics, streamline topology and interfacial stresses due to a drop in shear," J. Fluid Mech. **683**, 149 (2011).
[18]K. S. Sheth and C. Pozrikidis, "Effects of inertia on the deformation of liquid drops in simple shear flow," Comput. Fluids **24**, 101 (1995).
[19]D. B. Khismatullin, Y. Renardy, and V. Cristini, "Inertia-induced breakup of highly viscous drops subjected to simple shear," Phys. Fluids **15**, 1351 (2003).
[20]Y. Renardy, V. Cristini, and J. Li, "Drop fragment distributions under shear with inertia," Int. J. Multiphase Flow **28**, 1125 (2002).
[21]Y. Renardy, "The effects of confinement and inertia on the production of droplets," Rheol. Acta **46**, 521 (2007).
[22]S. Farokhirad, T. Lee, and J. F. Morris, "Effects of inertia and viscosity on single droplet deformation in confined shear flow," Commun. Comput. Phys. **13**, 706 (2013).
[23]X. Li and K. Sarkar, "Effects of inertia on the rheology of a dilute emulsion of drops in shear," J. Rheol. **49**, 1377 (2005).
[24]R. Andersson and B. Andersson, "On the breakup of fluid particles in turbulent flows," AIChE J. **52**, 2020 (2006).
[25]S. Galinat, L. Garrido Torres, O. Masbernat, P. Guiraud, F. Risso, C. Dalmazzone, and C. Noik, "Breakup of a drop in a liquid–liquid pipe flow through an orifice," AIChE J. **53**, 56 (2007).
[26]E. H. Herø, N. La Forgia, J. Solsvik, and H. A. Jakobsen, "Single drop breakage in turbulent flow: Statistical data analysis," Chem. Eng. Sci.: X **8**, 100082 (2020).
[27]N. La Forgia, E. H. Herø, and H. A. Jakobsen, "High-speed image processing of fluid particle breakage in turbulent flow," Chem. Eng. Sci.: X **12**, 100117 (2021).
[28]A. U. M. Masuk, A. K. Salibindla, and R. Ni, "The orientational dynamics of deformable finite-sized bubbles in turbulence," J. Fluid Mech. **910**, A21 (2021).
[29]J. Solsvik and H. A. Jakobsen, "Single drop breakup experiments in stirred liquid–liquid tank," Chem. Eng. Sci. **131**, 219 (2015).
[30]S. Tcholakova, N. D. Denkov, and T. Danner, "Role of surfactant type and concentration for the mean drop size during emulsification in turbulent flow," Langmuir **20**, 7444 (2004).
[31]A. Komrakova, O. Shardt, D. Eskin, and J. Derksen, "Effects of dispersed phase viscosity on drop deformation and breakup in inertial shear flow," Chem. Eng. Sci. **126**, 150 (2015).
[32]N. Vankova, S. Tcholakova, N. D. Denkov, I. B. Ivanov, V. D. Vulchev, and T. Danner, "Emulsification in turbulent flow: 1. Mean and maximum drop diameters in inertial and viscous regimes," J. Colloid Interface Sci. **312**, 363 (2007).
[33]R. D'Apolito, A. Perazzo, V. Preziosi, M. D'Antuono, G. Tomaiuolo, R. Miller, and S. Guido, "Measuring interfacial tension of emulsions in situ by microfluidics," Langmuir **34**, 4991 (2018).
[34]V. Preziosi, A. Perazzo, G. Tomaiuolo, V. Pipich, D. Danino, L. Paduano, and S. Guido, "Flow-induced nanostructuring of gelled emulsions," Soft Matter **13**, 5696 (2017).

[35]F. De Vita, M. E. Rosti, S. Caserta, and L. Brandt, "On the effect of coalescence on the rheology of emulsions," J. Fluid Mech. **880**, 969 (2019).
[36]R. Graziano, V. Preziosi, D. Uva, G. Tomaiuolo, B. Mohebbi, J. Claussen, and S. Guido, "The microstructure of Carbopol in water under static and flow conditions and its effect on the yield stress," J. Colloid Interface Sci. **582**, 1067 (2021).
[37]X. Li and C. Pozrikidis, "The effect of surfactants on drop deformation and on the rheology of dilute emulsions in Stokes flow," J. Fluid Mech. **341**, 165 (1997).
[38]S. O. Unverdi and G. Tryggvason, "A front-tracking method for viscous, incompressible, multi-fluid flows," J. Comput. Phys. **100**, 25 (1992).
[39]C. S. Peskin, "Numerical analysis of blood flow in the heart," J. Comput. Phys. **25**, 220 (1977).
[40]X. Li and K. Sarkar, "Drop dynamics in an oscillating extensional flow at finite Reynolds numbers," Phys. Fluids **17**, 027103 (2005).
[41]K. Sarkar and W. R. Schowalter, "Deformation of a two-dimensional viscoelastic drop at non-zero Reynolds number in time-periodic extensional flows," J. Non-Newtonian Fluid Mech. **95**, 315 (2000).
[42]S. Mukherjee, A. Tarafder, A. R. Malipeddi, and K. Sarkar, "Shear-induced migration of a viscous drop in a viscoelastic liquid near a wall at high viscosity ratio: Reverse migration," J. Non-Newtonian Fluid Mech. **301**, 104751 (2022).
[43]A. R. Malipeddi, A. Tarafder, and K. Sarkar, "Deformation and breakup of a viscoelastic drop in time-dependent extensional flows with finite inertia," J. Non-Newtonian Fluid Mech. **321**, 105108 (2023).
[44]A. Tarafder, A. R. Malipeddi, and K. Sarkar, "Pair interactions between viscous drops in a viscoelastic matrix in free shear: Transition from passing to tumbling trajectories," J. Rheol. **66**, 571 (2022).
[45]S. Guido and M. Villone, "Three-dimensional shape of a drop under simple shear flow," J. Rheol. **42**, 395 (1998).
[46]A. S. Almusallam, R. G. Larson, and M. J. Solomon, "A constitutive model for the prediction of ellipsoidal droplet shapes and stresses in immiscible blends," J. Rheol. **44**, 1055 (2000).
[47]G. G. Poe and A. Acrivos, "Closed-streamline flows past rotating single cylinders and spheres: Inertia effects," J. Fluid Mech. **72**, 605 (1975).
[48]D. R. Mikulencak and J. F. Morris, "Stationary shear flow around fixed and free bodies at finite Reynolds number," J. Fluid Mech. **520**, 215 (2004).
[49]P. O. Olapade, R. K. Singh, and K. Sarkar, "Pairwise interactions between deformable drops in free shear at finite inertia," Phys. Fluids **21**, 063302 (2009).
[50]S. Guido and M. Simeone, "Binary collision of drops in simple shear flow by computer-assisted video optical microscopy," J. Fluid Mech. **357**, 1–20 (1998).
[51]V. Cristini, R. Hooper, C. Macosko, M. Simeone, and S. Guido, "A numerical and experimental investigation of Lamellar blend morphologies," Ind. Eng. Chem. Res. **41**, 6305 (2002).
[52]S. Torza, R. Cox, and S. Mason, "Particle motions in sheared suspensions XXVII. Transient and steady deformation and burst of liquid drops," J. Colloid Interface Sci. **38**, 395 (1972).